

# A model for Joule heating-induced dispersion in microchip electrophoresis

Yi Wang,<sup>a</sup> Qiao Lin\*<sup>a</sup> and Tamal Mukherjee<sup>b</sup>

<sup>a</sup>Department of Mechanical Engineering, Carnegie Mellon University, Pittsburgh, Pennsylvania, 15213, USA. E-mail: qlin@andrew.cmu.edu; Fax: 412-268-3348; Tel: 412-268-3641

<sup>b</sup>Department of Electrical and Computer Engineering, Carnegie Mellon University, Pittsburgh, Pennsylvania, 15213, USA

Received 6th May 2004, Accepted 2nd August 2004

First published as an Advance Article on the web 21st October 2004

This paper presents an analytical and parameterized model for analyzing the effects of Joule heating on analyte dispersion in electrophoretic separation microchannels. We first obtain non-uniform temperature distributions in the channel resulting from Joule heating, and then determine variations in electrophoretic velocity, based on the fact that the analyte's electrophoretic mobility depends on the buffer viscosity and hence temperature. The convection–diffusion equation is then formulated and solved in terms of spatial moments of the analyte concentration. The resulting model is validated by both numerical simulations and experimental data, and holds for all mass transfer regimes, including unsteady dispersion processes that commonly occur in microchip electrophoresis. This model, which is given in terms of analytical expressions and fully parameterized with channel dimensions and material properties, applies to dispersion of analyte bands of general initial shape in straight and constant-radius-turn channels. As such, the model can be used to represent analyte dispersion in microchannels of more general shape, such as serpentine- or spiral-shaped channels.

## 1 Introduction

Electrophoretic separation microchips have been actively pursued in the past decade,<sup>1–6</sup> and hold great promise for a wide spectrum of applications in biology and chemistry.<sup>7,8</sup> By performing separations in microchannels that are integrated with other microfluidic components, microchip electrophoresis is a key technology to enable lab-on-a-chip microsystems that integrate chemical analysis with other bioanalytical functionalities.<sup>7,8</sup> While microchip electrophoresis is of great importance, the creation of such devices that have optimized geometry and performance and are suitable for specific applications is still an art, requiring long development cycle times. This is in a large part due to a lack of models that are accurate to capture the physics of electrophoretic separation, and yet efficient to allow fast evaluation of candidate designs in the chip design process. This paper addresses this issue by presenting a parameterized model for analyzing analyte dispersion caused by Joule heating effects in electrophoresis microchannels.

In electrophoresis, an electric field is used to drive a band of charged analyte molecules through a microchannel filled with a conducting buffer. Different species in the analyte are thereby separated by their different electrophoretic mobilities. This process, however, is accompanied by the resistive heating, or Joule heating (JH), of the buffer as the electric field also induces a current. Joule heating leads to non-uniformities in the buffer temperature and electrophoretic mobility, which contribute to dispersion of the analyte transport. Joule heating can be significant in the presence of high electric fields, which are desired for improving electrophoretic separation speed and resolving power.<sup>9,10</sup> There can also be appreciable Joule heating in microchannels of relatively large cross-sectional dimensions, which are at times used to allow longer detection cells, higher detectability, reduced adsorption of analytes to channel walls, and less stringent requirements on sample injection schemes.<sup>11</sup> It is therefore important to develop models

that account for the effects of Joule heating on analyte dispersion to allow optimal design of electrophoretic separation microchips.

Closed-form and parameterized models are highly desirable for describing dispersion in microchip electrophoresis, as they provide computational efficiency appropriate for use in iterative design processes to explore the parameter space.<sup>12,13</sup> Taylor<sup>14,15</sup> and Aris<sup>16</sup> pioneered studies of dispersion phenomena by considering dispersion of a solute in a hydrodynamically driven flow in a circular capillary, and developed the classical Taylor–Aris theory in which dispersion at large analyte migration time (*i.e.*, steady state) is represented by a constant dispersion coefficient. This theory has been used extensively in capillary electrophoresis. In particular, Knox and Grant<sup>17,18</sup> investigated JH-induced Taylor–Aris dispersion of electrophoresis in a circular capillary, while Cifuentes and Poppe<sup>19</sup> studied steady-state JH-induced dispersion in a rectangular capillary that is assumed to have an infinitely large aspect ratio. In the context of microchip electrophoresis, Molho<sup>10</sup> presented an analytical and steady-state model for JH-induced dispersion in rectangular channels that is based on models developed for circular capillaries. For electrophoresis in a constricted turn, he also investigated dispersion effects of Joule heating and turn curvature at specific regimes, which were assumed to be decoupled. Jacobson *et al.*<sup>9</sup> used the results of Knox and Grant for the capillaries to evaluate Joule heating dispersion effects in rectangular microchannels. It is important, however, to note that in microchip-based electrophoretic separations, dispersion is often not in steady state due to short analyte residence times in the channel. The use of steady-state dispersion models for unsteady dispersion, as well as approximation of rectangular channels by capillaries, in general leads to significant errors. Unsteady dispersion in rectangular channels has been investigated by Doshi *et al.*<sup>20</sup> in the context of a gravity-driven hydrodynamic flow. They found that such dispersion involves three stages characterized by diffusion time constants along the two cross-sectional dimensions, and differs distinctly from

dispersion in a hydrodynamic flow between two parallel plates, as further discussed by Dorfman and Brenner.<sup>21</sup>

We present an analytical model for Joule heating-induced analyte dispersion in electrophoretic separation microchannels. JH-induced variations in temperature and electrophoretic velocity in the channel are first obtained to establish the mass transfer equation, which is then formulated in terms of spatial moments of analyte concentration<sup>16</sup> (Section 2). The equation is solved to yield an analytical and parameterized model for JH-induced dispersion, which holds for analyte bands of general initial shape in both straight channels and constant-radius turns (Section 3). The model is validated with experimental data and full numerical simulation results, and employed to investigate the influence of geometrical and operational parameters on JH-induced dispersion in both straight channels (Section 4) and turns (Section 5). A summary of the paper and a brief discussion of future work are finally presented (Section 6).

## 2 Governing equations

This section presents the governing equations for dispersion, in the presence of Joule heating, of electrophoretic transport of a charged analyte in a microchannel. The microchannel is bounded by a pair of planes parallel to the chip surface, and a second pair of planes or a pair of concentric circular cylindrical surfaces perpendicular to the chip surface (Fig. 1). The channel hence has constant rectangular cross sections with width  $w$ , height  $h$ , and aspect ratio  $\beta = w/h$ . The line connecting the cross-sectional centers (the channel axis) is straight with length  $L$ , or a circular arc with average radius  $R$ , included angle  $\varphi$ , and length  $L = R\varphi$ . In the latter case the channel is called a constant-radius turn, and it is assumed that the *width-to-radius ratio is small*:  $b \triangleq w/R \ll 1$ . We also assume that *the channel is long*, i.e.  $w/L \ll 1$  and  $h/L \ll 1$ . These straight and constant-radius turn geometries are sufficiently general to be used to represent the majority of general-shaped microchannels that are commonly seen in practice.<sup>22</sup>

The electrophoresis of the analyte band is considered in the coordinate frame as shown in Fig. 1. The governing equations will be given for a constant radius-turn, which, when  $b = 0$ , reduces to the special case of a straight channel. Given a voltage  $V$  applied across the length of the channel, it can be shown that the electric field is approximately given by<sup>22,23</sup>

$$(E_x, E_y, E_z) = (E_0[1 + b(1/2 - z/h)], 0, 0) \quad (1)$$

where  $E_0 = V/L$ . That is, the electric field, directed along the channel axis, is constant in a straight channel, and varies linearly across the width of a turn.

The electric field induces a current in the conducting buffer generating Joule heating power<sup>17,18</sup>

$$\dot{q} = \rho E^2 \quad (2)$$

where  $\rho$  is the buffer's electric conductivity. JH will cause temperature variations within the microchannel. Such

temperature variations can be assumed in steady state, as the time required for the buffer to reach thermal equilibrium within the channel is generally much smaller than the characteristic diffusion time. For example, for a channel ( $h = 50 \mu\text{m}$ ) filled with an aqueous buffer, its thermal time constant is  $\sim 1.8 \times 10^{-3}$  s, which is 100 fold less than the transverse diffusion time ( $\sim 2.5 \times 10^{-1}$  s) of an ion species ( $D \sim 1 \times 10^{-9} \text{m}^2 \text{s}^{-1}$ ). In addition, as the channel length is much larger than the cross-sectional dimensions, the temperature distribution can be assumed to be independent of the axial coordinate  $x$ . Thus, by neglecting terms of order  $b^2$  or higher,<sup>23</sup> the steady-state heat transfer problem is governed by a two-dimensional equation:

$$\frac{\partial^2 \theta}{\partial y^2} + \frac{\partial^2 \theta}{\partial z^2} = -\frac{\dot{q}}{k} \quad (3)$$

where  $\theta = T - T_w$ ,  $T$  is the buffer temperature,  $T_w$  is the buffer temperature at the channel wall, and  $k$  is the buffer's thermal conductivity. Here, to a first approximation,  $T_w$  is taken to be uniform everywhere on the channel wall. This approximation is valid especially when the substrate is a good thermal conductor (e.g., silicon) or the microchannel has a large aspect ratio ( $\beta \gg 1$ , so that the temperature non-uniformity only occupies a small portion of the cross sectional perimeter and around the channel corner). In this case  $\theta = 0$  everywhere on the channel wall.

The effect of Joule heating on electrophoretic transport is primarily manifested *via* the temperature dependence of the buffer viscosity  $\eta$ . Within temperature ranges relevant to microchip electrophoresis, the viscosity is approximately linear in temperature:  $\eta = \eta_w(1 - \alpha\theta)$ , where  $\eta_w$  is the buffer viscosity at the channel wall, and  $\alpha$  is the buffer's temperature coefficient of viscosity.<sup>17,18</sup> The electrophoretic mobility of the analyte is given by  $\mu = a\epsilon\zeta/\eta$ , where  $\epsilon$  is the permittivity of the buffer,  $\zeta$  the zeta potential and  $a$  a constant.<sup>18</sup> It has been experimentally shown that  $\epsilon\zeta$  is independent of temperature.<sup>24</sup> Therefore  $\mu$  depends on temperature only *via* the temperature dependence of viscosity. When  $\alpha\theta \ll 1$ , we approximately have  $\mu = \mu_w(1 + \alpha\theta)$ , where  $\mu_w = a\epsilon\zeta/\eta_w$ . It follows that the electrophoretic velocity, given by  $(v_x, v_y, v_z) = (\mu E_x, 0, 0)$ ,<sup>10,17-19</sup> is non-uniform over the channel's cross section, and causes dispersion of analyte transport. The combined effect of JH and turn geometry on dispersion is represented by an apparent axial analyte velocity  $u_x = v_x(1 - b(1/2 - z/h))$ .<sup>23</sup> For convenience we use a dimensionless frame  $\xi = (x - Ut)/h$ ,  $\eta = y/h$  and  $\zeta = z/h$ , which moves with the average apparent analyte velocity  $U = u_{w,0}(1 + \alpha)$ , and a dimensionless time  $\tau = Dt/h^2$ . Here  $u_{w,0} = \mu_w E_0$  and the overbar denotes cross-sectional average. The convection-diffusion equation, which governs the dispersion process, then takes the form<sup>22</sup>

$$\begin{aligned} \frac{\partial c}{\partial \tau} &= \frac{\partial^2 c}{\partial \xi^2} + \frac{\partial^2 c}{\partial \eta^2} + \frac{\partial^2 c}{\partial \zeta^2} - Pe\chi \frac{\partial c}{\partial \xi} \\ \partial c / \partial \eta|_{\eta=0,1} &= 0, \quad \partial c / \partial \zeta|_{\zeta=0,\beta} = 0, \quad c|_{\tau=0} = c(\xi, \eta, \zeta, 0) \end{aligned} \quad (4)$$

where  $c$  is the analyte concentration,  $Pe = Uh/D$  is the Peclet number representing the ratio of convection and diffusion

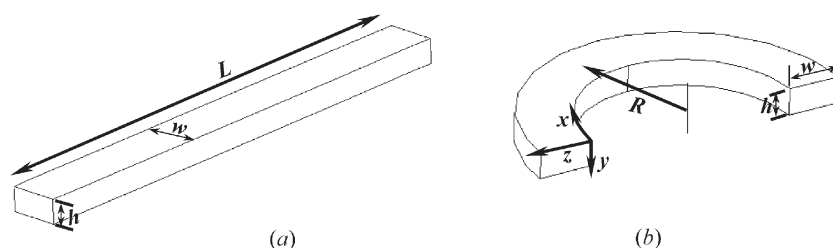


Fig. 1 Geometry and coordinate frame for (a) a straight channel and (b) a semi-circular turn.

transport rates. Here,  $\chi$  is the normalized apparent analyte velocity with respect to the average  $U$  and is given by

$$\chi(\eta, \zeta) = \frac{u_x(\eta, \zeta) - U}{U} = \begin{cases} \varepsilon(\phi - \bar{\phi}) / (1 + \varepsilon\bar{\phi}) & \text{for a straight channel} \\ \left[ \varepsilon(\phi - \bar{\phi}) + b(1 - 2\zeta/\beta) \right] / (1 + \varepsilon\bar{\phi}) & \text{for a turn} \end{cases} \quad (5)$$

where  $\varepsilon = \alpha(\rho E_0^2 h^2 / k)$  and  $\phi = \theta / (\rho E_0^2 h^2 / k) = \alpha\theta / \varepsilon$ , which can be found from eqns. (1)–(3). From these equations we also note that  $\rho E_0^2 h^2 / k$  is a characteristic temperature due to JH. Therefore the dimensionless parameter  $\varepsilon$  is the characteristic of JH intensity and will be hereafter called the Joule heating coefficient. Also note that  $\sqrt{\varepsilon}$  can be thought of as a dimensionless electric field strength. The dimensionless variable  $\phi$ , which depends only on the dimensionless curvature  $b$  and aspect ratio  $\beta$  (Section 3), can be interpreted as the normalized buffer temperature. Terms of the second or higher order in  $b$  and  $\alpha$  have been neglected for a turn in eqn. (5).

Eqn. (4) can be formulated in closed form in terms of spatial moments of the analyte concentration.<sup>10,16</sup> Specifically, if the entire analyte band is contained in the channel, eqn. (4) holds effectively for  $-\infty < \zeta < \infty$  such that  $c \rightarrow 0$  as  $\zeta \rightarrow \pm\infty$ . Define

$$c_p(\eta, \zeta, \tau) = \int_{-\infty}^{\infty} \zeta^p c(\zeta, \eta, \zeta, \tau) d\zeta \quad \text{and} \quad m_p(\tau) = \bar{c}_p = \frac{1}{\beta} \int_0^\beta \int_0^1 c_p d\eta d\zeta \quad (p=0, 1, 2, \dots) \quad (6)$$

where  $c_p$  is the  $p$ th moment of the concentration in a longitudinal filament of the analyte band that intersects the cross sections at  $\eta$  and  $\zeta$ , and  $m_p$  is the  $p$ th moment of the cross-sectional average concentration, respectively. Eqn. (4) can be integrated with respect to  $\zeta$  to yield

$$\begin{aligned} \frac{\partial c_p}{\partial \tau} &= \frac{\partial^2 c_p}{\partial \eta^2} + \frac{\partial^2 c_p}{\partial \zeta^2} + p(p-1)c_{p-2} + pPe\chi c_{p-1} \\ \frac{\partial c_p}{\partial \eta} \Big|_{\eta=0,1} &= 0, \quad \frac{\partial c_p}{\partial \zeta} \Big|_{\zeta=0,\beta} = 0, \quad c_p \Big|_{\tau=0} = c_{p0}(\eta, \zeta) = \int_{-\infty}^{\infty} c(\zeta, \eta, \zeta, 0) \zeta^p d\zeta. \end{aligned} \quad (7)$$

which can be further integrated over the cross section to obtain

$$\begin{aligned} \frac{dm_p}{d\tau} &= p(p-1)\bar{c}_{p-2} + pPe\bar{\chi}c_{p-1} \\ m_p(0) &= m_{p0} = \frac{1}{\beta} \int_0^\beta \int_0^1 c_{p0}(\eta, \zeta) d\eta d\zeta \end{aligned} \quad (8)$$

In both eqns. (7) and (8), any term that contains  $c_i$  with  $i < 0$  is set to zero. To determine the broadening of the analyte band, these equations can be solved to obtain moments up to the second order. Then,  $c_0(\eta, \zeta, \tau)$  is the analyte mass in the longitudinal analyte filament at  $\eta$  and  $\zeta$ , while  $m_0(\tau)$  is the total analyte mass in the channel. Next,  $c_1(\eta, \zeta, \tau)$  is the  $\zeta$ -coordinate of the centroid of the longitudinal analyte filament at  $\eta$  and  $\zeta$ , and hence indicates the skew of the analyte band.  $m_1(\tau)$ , the cross-sectional average of  $c_1$ , is the  $\zeta$ -coordinate of the centroid of the entire analyte band. Finally,  $m_2(\tau)$  is used to determine the variance of the analyte band (next section).

It should be noted that in addition to the electrophoretic mobility  $\mu$ , other material properties, such as the buffer's electric conductivity  $\rho$ , thermal conductivity  $k$ , and the analyte diffusivity  $D$ , in general also vary with temperature gradients within the channel through the temperature dependence of the buffer viscosity. However, the temperature dependence of these

parameters influences dispersion less significantly than the temperature dependence of  $\mu$ . For example, from eqns. (2) and (3), the non-uniform component of Joule heating, due to the temperature dependence of  $\rho$  and  $k$ , is generally small compared with the total Joule heating. In addition, from a more general form of the convection-diffusion equation,<sup>25</sup> it can be shown that the effect on dispersion of temperature dependence of  $D$ , compared with that of temperature dependence of  $\mu$ , is of second order. Therefore, it is reasonable to assume, as in the formulation above, that all material properties except  $\mu$  are constant<sup>17,18</sup> and can be evaluated at the average buffer temperature in the channel.

### 3 Joule heating dispersion model

This section presents analytical models for dispersion of electrophoretic transport in the presence of Joule heating. These models are obtained by first solving eqn. (3) for cross-sectional temperature distributions. Eqn. (5) then provides the electrophoretic velocity profile, which can be used in solving eqns. (7) and (8) for the moments of analyte concentration and hence the dispersion characteristics of the analyte band.

The normalized buffer temperature  $\phi$ , introduced with eqn. (5), can be found from eqns. (1)–(3):

$$\phi = (1+b)\phi_1 + \frac{2b\phi_2}{\beta} \quad (9)$$

where

$$\begin{aligned} \phi_1 &= \frac{1}{2} \left\{ \frac{1}{4} - \left( \eta - \frac{1}{2} \right)^2 + \sum_{i=1}^{\infty} \frac{(-1)^i \cosh(\kappa_i(2\zeta - \beta))}{\kappa_i^3} \frac{\cos(\kappa_i(2\eta - 1))}{\cosh(\kappa_i\beta)} \right\} \\ \phi_2 &= \sum_{i=1}^{\infty} \frac{2\beta(-1)^{i+1}}{i\pi\lambda_i} \left( -1 + \frac{e^{(1-\eta)\sqrt{\lambda_i}} + e^{\eta\sqrt{\lambda_i}}}{1 + e^{\sqrt{\lambda_i}}} \right) \sin\left(\frac{i\pi\zeta}{\beta}\right) \end{aligned}$$

with  $\kappa_i = (2i - 1)\pi/2$  and  $\lambda_i = (i\pi/\beta)^2$  ( $i = 1, 2, 3, \dots$ ).

The normalized velocity profile  $\chi$  is then obtained from eqn. (5) and substituted into eqns. (7) and (8), which can be solved for the moments of analyte concentration. The solution procedure has been outlined elsewhere,<sup>22</sup> with the difference being that  $\chi$  here includes JH velocity contribution and varies in both cross-sectional dimensions. First, by conservation of mass,  $m_0$  is constant. We choose  $m_0 = 1$  without loss of generality. In addition,

$$c_0(\eta, \zeta, \tau) = \int_{-\infty}^{\infty} c(\zeta, \eta, \zeta, \tau) d\zeta = 1 \quad (10)$$

provided the initial condition is such that  $\int_{-\infty}^{\infty} c(\zeta, \eta, \zeta, 0) d\zeta = 1$ . This indicates that if all longitudinal analyte band filaments have the same mass initially, then this will be the case at all times. This is typically true in practice and will be assumed in the remainder of this paper. For example, this is the case for an analyte band that is initially a uniform rectangular plug (in a straight channel or a turn).

For the first moment, it can then be found that  $m_1(\tau) = 0$  if the origin of the moving frame is chosen such that it initially coincides with the analyte band's centroid. Thus, the centroid and the moving origin coincide at all times if they do so initially. The first moment  $c_1$ , which represents the skew of the analyte band, is found to be

$$c_1(\eta, \zeta, \tau) = \sum_{m=0}^{\infty} \sum_{n=0}^{\infty} S_{nm}(\tau) \cos(n\pi\eta) \cos\left(\frac{m\pi\zeta}{\beta}\right) \quad (11)$$

where  $S_{00}(\tau) = S_{00}(0)$  and

$$S_{nm}(\tau) = S_{nm}(0)e^{-\lambda_{nm}\tau} + \frac{Pe\chi_{nm}(1 - e^{-\lambda_{nm}\tau})}{\lambda_{nm}} \quad \text{if } n+m \geq 1, \quad (12)$$

with  $S_{nm}(0) = v_{nm} \int_0^\beta \int_0^1 c_{10}(\eta, \zeta) \cos(n\pi\eta) \cos(m\pi\zeta/\beta) d\eta d\zeta$  and  $\lambda_{nm} = (n\pi)^2 + (m\pi/\beta)^2$  ( $n \geq 0$  and  $m \geq 0$ ). Here,  $v_{nm}$  is defined as  $v_{00} = 1/\beta$ ,  $v_{0m} = 2/\beta$ ,  $v_{n0} = 2/\beta$  and  $v_{nm} = 4/\beta$  for  $n > 1$  and  $m > 1$ ,  $c_{10}$  is the initial skew (eqn. (7)). The Fourier coefficients for the normalized velocity  $\chi$  are  $\chi_{00} = 0$ ,  $\chi_{0m} = \varepsilon\phi_{0m} + 4b(1 - (-1)^m)/\lambda_m$ ,  $\lambda_m = (m\pi)^2$ ,  $\chi_{nm} = \varepsilon\phi_{nm}$ ,  $\phi_{nm} = v_{nm} \int_0^\beta \int_0^1 \phi \cos(n\pi\eta) \cos(m\pi\zeta/\beta) d\eta d\zeta$ ,  $n \geq 0$  and  $m \geq 0$ .

The second-order moment  $m_2$  can be found by solving eqn. (8) with  $p = 2$ . Then, the relationship  $\sigma^2 = h^2 (m_2/m_0 - m_1^2/m_0^2)^{10}$  yields the variance of the analyte band:

$$\begin{aligned} \frac{\Delta\sigma^2(\tau)}{h^2} = & 2\tau + \sum_{\substack{n=0 \\ n+m \geq 1}}^{\infty} \sum_{m=0}^{\infty} \frac{2S_{nm}(0)Pe\chi_{nm}(1 - e^{-\lambda_{nm}\tau})}{\beta v_{nm}\lambda_{nm}} + \\ & \sum_{\substack{n=0 \\ n+m \geq 1}}^{\infty} \sum_{m=0}^{\infty} \frac{2\varepsilon^2 Pe^2 \phi_{nm}^2 (e^{-\lambda_{nm}\tau} + \lambda_{nm}\tau - 1)}{(1 + \varepsilon\bar{\phi})^2 \beta v_{nm}\lambda_{nm}^2} + \\ & \sum_{m=1,3,5,\dots}^{\infty} \frac{64b^2 Pe^2 (e^{-\lambda_{0m}\tau} + \lambda_{0m}\tau - 1)}{(1 + \varepsilon\bar{\phi})^2 \lambda_{0m}^2 \lambda_m^2} + \\ & \sum_{m=1,3,5,\dots}^{\infty} \frac{16\varepsilon b Pe^2 \phi_{0m} (e^{-\lambda_{0m}\tau} + \lambda_{0m}\tau - 1)}{(1 + \varepsilon\bar{\phi})^2 \lambda_{0m}^2 \lambda_m} \end{aligned} \quad (13)$$

where  $\Delta\sigma^2(\tau) = \sigma^2(\tau) - \sigma^2(0)$ , and  $\sigma^2(\tau)$  and  $\sigma^2(0)$  are the analyte band variance at time  $\tau$  and 0, respectively. It can be seen from the right-hand side of this equation that the increase in variance consists of contributions from molecular diffusion (the first term), the initial skew (the second term), Joule heating effects (the third term), turn geometry (the fourth term), and interactions between Joule heating and turn geometry (the last term). To our knowledge this is the first time these interactions are considered in microchip electrophoresis models in all mass regimes and in a coupled manner.

We now consider several special cases of electrophoretic transport. First, note that if  $\varepsilon \ll 1$ , eqn. (13) indicates that Joule heating can be ignored. Analyte band broadening will then be exclusively caused by diffusion and turn geometry, and the details of this case have been discussed in ref. 22 Next, the Joule heating dispersion model can be considerably simplified for straight channels ( $b = 0$ ) when no initial skew is involved; and this case has been thoroughly discussed in ref. 26

Eqn. (13) shows the evolution of the band spreading within the channels. In practice, chip designers are primarily interested in the resolving power at the outlet of the electrophoresis channel. Therefore, we introduce the plate number<sup>27,28</sup>

$$N = \frac{L^2}{\sigma^2(\tau_f)} \quad (14)$$

and the dimensionless residence time

$$\tau_f = t_f D/h^2 = (L/h)/Pe \quad (15)$$

where  $L$  is the length of the separation channel ( $L = \phi R = \phi\beta h/b$  for a turn), and  $t_f = L/U$  is the dimensional residence time of the centroid of the analyte band in the channel. The plate number can be interpreted as a normalized measure of resolving power of an electrophoretic separation system, or in the context of this paper, a component channel in such a system.

We have thus derived an analytical model for dispersion due to Joule heating by focusing on electrophoresis. JH-induced dispersion in electroosmotic flow (EOF) is not considered in the model, but may be addressed by conceptually similar

approaches. In particular, for the special case of a straight channel, dispersion caused by EOF may actually be negligible if the electric double layer is thin compared with the channel cross-section dimensions,<sup>29</sup> if the channel wall temperature  $T_w$  is uniform (otherwise, additional dispersion due to the dependence of EOF mobility on temperature would need to be included). Then, the current model will still be valid if the moving frame is given velocity  $U + U_{eof}$ , where  $U_{eof}$  is the EOF velocity (which is uniform over the channel cross section) and the residence time in eqn. (15) is defined by  $\tau_f = LD/(U + U_{eof})h^2$ .

#### 4 Joule heating effects in straight channels

In this section, the analytical Joule heating dispersion model is first verified with numerical simulations as well as experimental data extracted from the literature.<sup>9</sup> Then, a parametric study is performed to investigate the dependence of JH-induced dispersion on the applied electric field, channel length and aspect ratio.

In Fig. 2, the JH dispersion model (eqn. (13)) for a straight channel is compared with experimental data,<sup>9</sup> where Rhodamine B (RB) and Dichlorofluorescein (DCF) (whose diffusivities and mobilities are given in ref. 9) are separated in a straight channel of dimensions  $200 \times 26 \times 7 \mu\text{m}^3$ . For consistency with experimental data,<sup>9</sup> the plate height  $H$ , defined as  $L/N$ , is employed here as a measure of resolving power. It can be seen that  $H$  obtained from the model is almost the same for RB and DCF. This is consistent with the experimental data, in which the RB and DCF plate heights do not differ significantly. The model-predicted and experimentally determined plate heights agree in the order of magnitude and exhibit the same trend in their dependence on electric field. The seemingly systematic deviation of the model from the experiment data could be attributed to uncertainties in the values of the geometric and material parameters given by the ref. 9 and non-uniform wall temperature distributions that caused additional dispersion due to non-uniform EOF (above).

The model-predicted evolution of the variance of an analyte band in a straight channel is also compared with numerical results. In this comparison, the channel is given a fixed width  $h = 50 \mu\text{m}$  with an aspect ratio  $\beta$  varying from 1 to 8. The following parameters are used:  $\sigma^2(0) = 3600 \mu\text{m}^2$  and  $S_{nm}(0) = 0$  ( $t = 0$  is the time instant when the band's centroid is at the channel entrance),  $E = 3.0 \text{ kV cm}^{-1}$ ,  $\mu_w = 2 \times 10^{-8} \text{ m}^2 \text{ V}^{-1} \text{ s}^{-1}$ ,  $k = 0.6 \text{ W m}^{-1} \text{ K}^{-1}$ ,  $\alpha = 0.025 \text{ K}^{-1}$ ,  $\rho = 0.1 \text{ S m}^{-1}$ , and  $D = 3.0 \times 10^{-10} \text{ m}^2 \text{ s}^{-1}$ . These values correspond to  $Pe = 1072$  and  $\varepsilon = 0.94$ . As shown in Fig. 3, excellent agreement can be observed between the analytical modeling and simulation

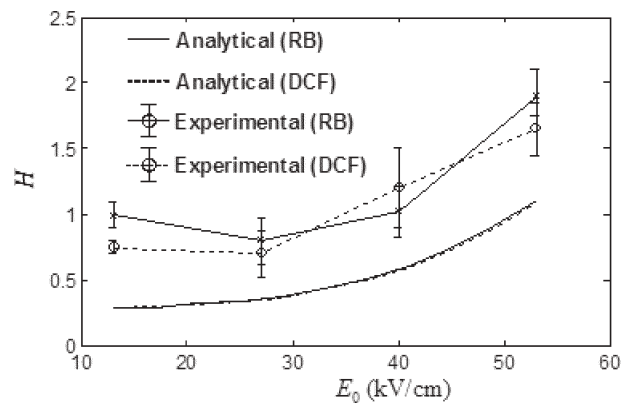
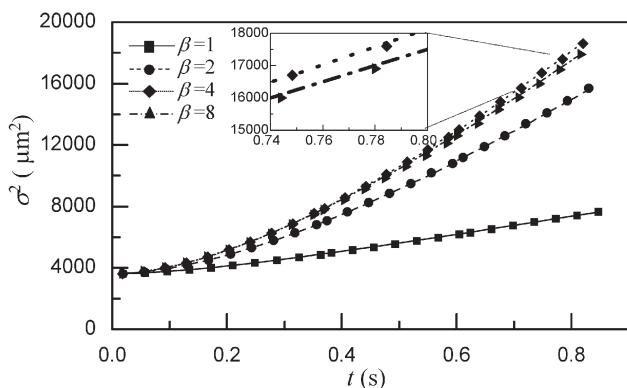


Fig. 2 Comparison of model-predicted and experimentally determined<sup>9</sup> plate height  $H$  for Rhodamine B (RB) and Dichlorofluorescein (DCF).



**Fig. 3** Comparison of variances computed from the analytical model (lines) and numerical simulations (symbols) in straight channels.

results (within 2%). We also observe that when  $t$  is fixed, both analytical and numerical results indicate that band broadening generally increases with  $\beta$ , but not in a monotonic manner. This is attributed to the role of transient dispersion and is explained below.

We now demonstrate the utility of the model by applying it to a parametric analysis of JH-induced dispersion in a straight channel. It can be shown from eqns. (14) and (15) that the plate number  $N$  depends on the parameters  $Pe$ ,  $\varepsilon$ ,  $L/h$  and  $\beta$  for a straight channel. For convenience of analysis and to aid intuition, we consider the effects of these parameters by examining the dependence of  $N$  on  $E_0$  as  $\beta$  (Fig. 4) or  $L/h$  (Fig. 5) is varied. In this parametric analysis, the values of  $\mu_w$ ,  $k$ ,  $\alpha$ ,  $\rho$  and  $D$  are the same as those used above in the numerical verification;  $\sigma^2(0) = 0$ ; and  $0.1 < E_0 < 3 \text{ kV cm}^{-1}$  (or correspondingly  $0.001 < \varepsilon < 0.94$ ). As shown in Fig. 4 (in which  $L/h = 100$  is fixed),  $N$  initially increases with  $E_0$  until achieving a maximum ( $N_{\max}$ ), and then decreases with  $E_0$ . In addition,  $N$  is virtually the same at sufficiently low  $E_0$  for all  $\beta$  considered. This is because at low electric fields, JH effects are negligible, and  $N$  is primarily determined by the effect of longitudinal molecular diffusion, which decreases with  $E_0$ . As  $E_0$  increases JH effects become increasingly significant and eventually dominate the dispersion, causing  $N$  to decrease. The value of  $N_{\max}$  varies with  $\beta$ , and is the largest ( $N_{\max} \approx 22800$ ) for  $\beta = 1$ . This is not surprising, as of all rectangular cross sections, the square shape allows the most efficient heat dissipation and minimized JH effects. While  $N_{\max}$  generally decreases with  $\beta$ , it is interesting to note that the decrease is not monotonic. For example,  $N_{\max}$  for  $\beta = 8$  is slightly higher than that for  $\beta = 4$ . This is because, as the band arrives at the channel exit (with the channel length fixed), dispersion has

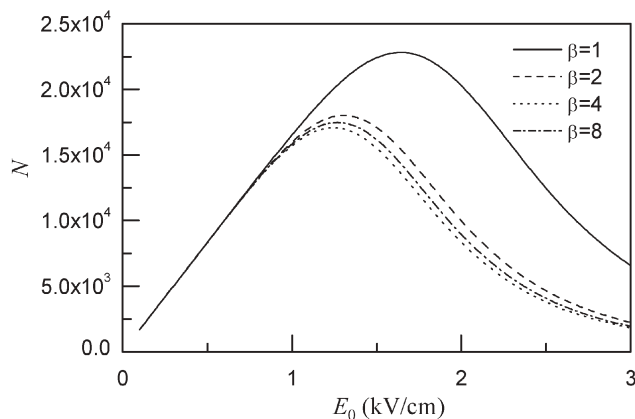


**Fig. 4** Dependence of the plate number  $N$  on average electric field  $E_0$  in a straight channel with different aspect ratios.

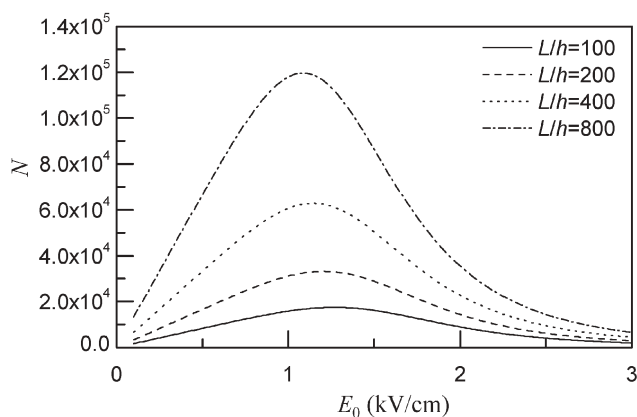


**Fig. 5** Dependence of the plate number  $N$  on average electric field  $E_0$  in a straight channel with different length-to-depth ratios.

reached steady state in both cross-sectional dimensions for  $\beta = 4$ , but is still in transient state in the width-wise dimension for  $\beta = 8$ , resulting in a variance smaller than the steady state variance for a lower aspect ratio.<sup>20,26</sup>

The effect of the dimensionless channel length  $L/h$  on the JH dispersion is quite straightforward and is shown in Fig. 5 (in which  $\beta = 8$  is fixed). For the reason explained above, the plate number  $N$  again exhibits a maximum as the electric field  $E_0$  increases. Additionally,  $N$  increases with  $L/h$ . This is expected, as a longer (or equivalently, shallower) channel leads to a larger separation of the species and hence increased resolving power. However, it is important to note that  $L/h$  cannot be infinitely increased to improve the separation performance, as it is not cost-effective to fabricate microchips with straight channels of overly large lengths.

## 5 Joule heating effects in turns

We consider JH-induced dispersion in constant radius-turns in this section. The relative significance of Joule heating with respect to diffusion and curvature effects will first be examined. Then, a parametric analysis of JH dispersion in turns will be performed, and results from the analytical model and numerical simulations will also be compared. We will continue to use the plate number  $N$  (eqn. (14) defined for a single turn), with the residence time  $\tau_f$  computed from eqn. (15). We will focus on turns with  $\varphi = \pi$  and an analyte band that is unskewed (e.g.,  $S_{mm}(0) = 0$ ) before its entry into the turn although the discussions can be readily extended to initially skewed bands in turns of different included angles. We choose  $D = 1 \times 10^{-9} \text{ m}^2 \text{ s}^{-1}$ ,  $\rho = 0.1 \text{ S m}^{-1}$ ,  $\mu_w = 2 \times 10^{-8} \text{ m}^2 \text{ V}^{-1} \text{ s}^{-1}$ ,  $k = 0.6 \text{ W m}^{-1} \text{ K}^{-1}$ ,  $\alpha = 0.025 \text{ K}^{-1}$ ,  $\sigma^2(0) = 0 \text{ } \mu\text{m}^2$  and  $S_{mm}(0) = 0$ .

First, the influence of JH-induced dispersion on the overall band broadening behavior is shown in Fig. 6. Here the plate number  $N$ , calculated with and without consideration of JH effects, is shown as a function of  $E_0$  for  $\beta = 1$ . The channel is given a depth  $h = 50 \text{ } \mu\text{m}$  and an average radius  $R = 2000 \text{ } \mu\text{m}$ . It can be seen that there exists a critical value of  $E_0$  at which  $N$  achieves a maximum ( $N_{\max}$ ) regardless of JH effects. However, while the turn curvature effects cause only a slight decrease of  $N$  from  $N_{\max}$ , the presence of significant Joule heating results in a rather pronounced drop in  $N$ . Thus, at relatively high electric fields, consideration of Joule heating is crucial for the accuracy of band broadening modeling. For example, the prediction of plate number  $N$  without considering JH dispersion leads to an error of 30% at  $E_0 = 3 \text{ kV cm}^{-1}$  ( $\varepsilon = 0.94$  and  $Pe = 322$ ). As  $E_0$  further increases to  $4 \text{ kV cm}^{-1}$  ( $\varepsilon = 1.67$  and  $Pe = 423$ ), this error is quadrupled, growing to 120%.

We now perform a parametric analysis of analyte band

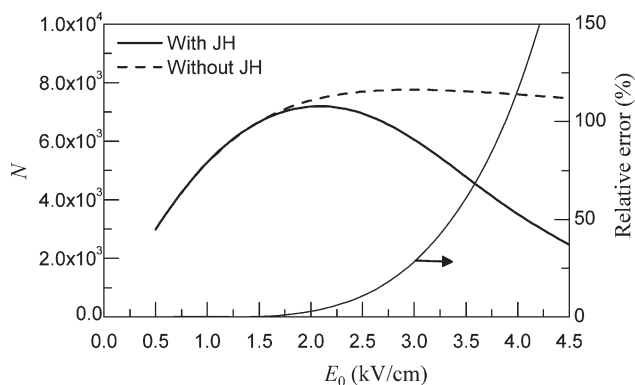


**Fig. 6** Comparison of the plate number  $N$  computed with and without consideration of Joule heating, as well as the relative error introduced without considering JH effects on  $N$ .

broadening in the presence of Joule heating. It can be shown that the effect of channel length (or equivalently, the average radius  $R$ ) is very similar to the straight channel case (Fig. 5), and will not be repeated here. Hence, we will fix  $R = 2000 \mu\text{m}$  along with  $h = 50 \mu\text{m}$ , and consider the influence of varying average electric field  $E_0$  and aspect ratio  $\beta$ , noting that the turn curvature is now uniquely determined by  $\beta$  through  $b = w/R = \beta(h/R)$ . As shown in Fig. 7, for a given  $E_0$  value,  $N$  increases with decreasing  $\beta$  because a more square cross-sectional shape allows more efficient dissipation of Joule heating. Differing from the straight channel case, this increase in  $N$  is, in addition to JH effects, also attributable to reduced curvature-induced velocity non-uniformities in the turn, as smaller  $\beta$  means smaller turn curvature  $b$ . Additionally, it can be seen that when  $E_0$  is sufficiently small (e.g.  $E_0 < 0.03 \text{ kV cm}^{-1}$ ),  $N$  increases virtually linearly with  $E_0$  and almost coincides for all  $\beta$ . This is because at low electric fields, both JH and curvature dispersion effects are negligibly small compared with longitudinal diffusion effects, which are independent of  $\beta$  (eqn. (13)). Thus, eqns. (13), (14) and (15) indicate that the  $N$  is approximately linearly proportional to the  $Pe$  number, and hence the electric field  $E_0$ . In contrast,  $N$  behaves quite differently at higher electric fields (e.g.  $0.03 \leq E_0 \leq 4 \text{ kV cm}^{-1}$ ). When  $\beta$  (and hence  $b$ ) is small (e.g.,  $\beta \leq 4$ )  $N$  is determined by the coupled effects of diffusion, JH and curvature-induced dispersion, with JH effects playing a more significant role than the curvature effects at a higher electric field (e.g.,  $E_0 = 3.5 \sim 4 \text{ kV cm}^{-1}$ ), as shown in Fig. 6.  $N$  initially increases with  $E_0$  until reaching a maximum (e.g.,  $N_{\text{max}} = 7200$  at  $E_0 = 2.1 \text{ kV cm}^{-1}$  for  $\beta = 1$ ), and then decreases due to JH and curvature-induced dispersion as  $E_0$  further increases. On the other hand, when  $\beta$  (and hence  $b$ ) is large, turn curvature-

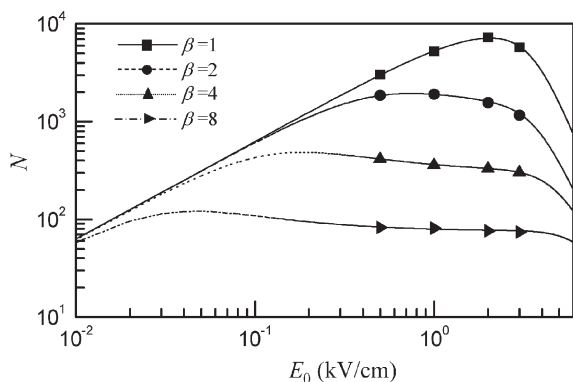


**Fig. 7** The dependence of the plate number  $N$  on the average electric field  $E_0$  for varying values of the aspect ratio  $\beta$  of a turn, as computed from the analytical model (lines) and numerical simulations (symbols).

induced velocity non-uniformities cause more dispersion than Joule heating. For example, when  $\beta = 8$ , curvature effects account for about 75% of band-broadening under an electric field of  $E_0 = 4 \text{ kV cm}^{-1}$ . Thus, compared with JH effects, curvature effects at large  $\beta$  results in a more significant reduction in the maximum plate number  $N_{\text{max}}$ , as well as the electric field at which  $N_{\text{max}}$  is achieved.

The plate number  $N$  obtained from full numerical simulations is also compared with the analytical modeling results in Fig. 7. When  $E_0 < 0.5 \text{ kV cm}^{-1}$  ( $\varepsilon < 0.02$ ), JH dispersion is negligible. The analytical dispersion model in this case (the 1st, 2nd and 4th terms in eqn. (13)) has been verified elsewhere experimentally and numerically.<sup>22</sup> Thus, the numerical simulations are here performed for  $0.5 < E_0 < 3 \text{ kV cm}^{-1}$  (or  $0.02 < \varepsilon < 0.94$ ), a practical range in which JH effects can be significant. It can be seen from the figure that there is good agreement between the analytical and numerical results. A worst-case error of 5.5% is observed for  $\beta = 8$  and  $E = 3 \text{ kV cm}^{-1}$  ( $Pe = 322$  and  $\varepsilon = 0.94$ ), and can be attributed to the relatively large curvature ( $b = 0.2$ ).

Finally, it is interesting to note that the analytical JH dispersion model has led to a drastic improvement in computational efficiency over full numerical simulations. The numerical simulations presented in Figs. 3 and 7 were performed, using a domain-wise approach,<sup>30</sup> in FEMLAB 3.0a<sup>30</sup> on a multi-user, 2-CPU 1-GHz Sun Fire 280 processor with 4 GB RAM. Computation of a single plate number value required from 6 h (for small  $\beta$  and  $E_0$  values) to four days (for the relatively large  $\beta$  and  $E_0$  values). In contrast, the analytical model required no more than a second of computation time to obtain a plate number value, and as such is suitable for use in simulations of complex electrophoretic separation systems.<sup>22</sup>

## 6 Conclusions

We have investigated Joule heating-induced analyte dispersion in electrophoretic separation microchannels. We considered non-uniform electrophoretic velocity distributions caused by Joule heating, and then obtained an analytical model for analyte dispersion, which is valid in all mass transfer regimes, and in particular can be used for unsteady dispersion processes that commonly occur in microchip electrophoresis. The model is given in terms of analytical expressions and fully parameterized with channel dimensions and material properties. It applies to analyte bands of general initial shape migrating in straight and constant-radius turn channels, and has been validated by both numerical simulations and experimental data. As such, the model can be used to represent analyte dispersion in microchannels of more general shape, such as serpentine- or spiral-shaped channels.<sup>22</sup>

The model has been used to study the effects of several key parameters on Joule heating-induced dispersion in both straight channels and turns. In straight channels, the dependence of the plate number, which characterizes the resolving power of separation, on electric field, channel's length-to-depth ratio and aspect ratio are analyzed. It is found that a maximum plate number can be achieved when the combined dispersion due to molecular diffusion and Joule heating dispersion is minimized. A long (or equivalently, shallow) channel is preferred for chip design because it generates less heat or (and) allows higher separation spacing between species.

Applying the model to a constant-radius-turn microchannel, we have considered the coupled dispersion effects of Joule heating and turn geometry. In particular, we investigated the influence on such a dispersion of the electric field, aspect ratio and turn curvature. It was shown that when the curvature is small, both Joule heating and turn curvature effects are

important in practically relevant ranges of electric fields. JH dispersion shows a more significant influence on separation performance than the curvature at high electric fields, while curvature-effects, as expected, increase with the turn curvature. Additionally, JH-induced dispersion, coupled with curvature-induced dispersion, increases with electric fields and eventually causes separation performance to deteriorate.

There are two aspects to be addressed in future work. First, in the current model, channel walls are assumed to be at uniform temperature. This first approximation considerably simplifies the formulation of the heat transfer problem in the model, and is accurate for substrates that are good thermal conductors or channels that have large aspect ratios. To improve the accuracy of the model for general substrates and channel aspect ratios, where there may be significant temperature variations on channel walls, heat transfer in the substrate as well as in the buffer will need to be accounted for. This consideration will also provide a more accurate knowledge of average buffer temperature, allowing accurate evaluation of average material properties for use in the model. Such a heat transfer problem will generally no longer admit an analytical solution. However, it may still be possible to obtain closed-form correlations that are fitted to numerical solutions expressed in appropriate dimensionless parameters.<sup>31</sup> The second aspect of future work concerns applying the Joule heating model to the design of complex electrophoretic systems, using the system simulation approach described in ref. 22 That is, a channel of complex shape can be decomposed into straight and turn elements, which are each described by the Joule heating model presented in this paper. These models then can be linked with the aid of appropriate parameters at interfaces of neighboring components, to represent the entire complex channel. This approach can be further extended to include other functional components such as reservoirs, mixers and reactors to efficiently simulate the complete electrokinetic microfluidic systems.

## Acknowledgements

This research is sponsored by DARPA and Air Force Research Laboratory, Air Force Material Command, USAF, under grant number F30602-01-2-0587, and the NSF ITR program under award number CCR-0325344. We appreciate helpful discussions with Drs. S. Hauan, J. Hoberg and S.C. Jacobson.

## References

- 1 D. J. Harrison, A. Manz, Z. H. Fan, H. Ludi and H. M. Widmer, *Anal. Chem.*, 1992, **64**, 1926–1932.

- 2 A. Manz, D. J. Harrison, E. M. J. Verpoorte, J. C. Fetting, A. Paulus, H. Ludi and H. M. Widmer, *J. Chromatogr.*, 1992, **593**, 253–258.
- 3 D. E. Raymond, A. Manz and H. M. Widmer, *Anal. Chem.*, 1994, **66**, 2858–2865.
- 4 C. S. Effenhauser, A. Paulus, A. Manz and H. M. Widmer, *Anal. Chem.*, 1994, **66**, 2949–2953.
- 5 A. T. Woolley and R. A. Mathies, *Anal. Chem.*, 1995, **67**, 3676–3680.
- 6 S. C. Jacobson, R. Hergenroder, L. B. Koutny and J. M. Ramsey, *Anal. Chem.*, 1994, **66**, 1114–1118.
- 7 D. R. Reyes, D. Lossifidis, P.-A. Auroux and A. Manz, *Anal. Chem.*, 2002, **74**, 2623–2636.
- 8 P. A. Auroux, D. Lossifidis, D. R. Reyes and A. Manz, *Anal. Chem.*, 2002, **74**, 2637–2652.
- 9 S. C. Jacobson, C. T. Culbertson, J. E. Daler and J. M. Ramsey, *Anal. Chem.*, 1998, **70**, 3476–3480.
- 10 J. I. Molho, PhD Thesis, Stanford University, 2001.
- 11 E. Grushka, R. M. McCormick and J. J. Kirkland, *Anal. Chem.*, 1989, **61**, 241–246.
- 12 Y. Wang, Q. Lin and T. Mukherjee, *Proceedings of Modeling and Simulation of Microsystems (MSM'04)*, Boston, MA, 2004, pp. 59–62.
- 13 A. J. Pfeiffer, T. Mukherjee and S. Hauan, *Proceedings of ASME International Mechanical Engineering Congress and RD&D Expo (IMECE 2003)*, Washington D.C., November 2003.
- 14 G. Taylor, *Proc. R. Soc. London, Ser. A*, 1953, **219**, 186–203.
- 15 G. Taylor, *Proc. R. Soc. London, Ser. A*, 1954, **225**, 473–477.
- 16 R. Aris, *Proc. R. Soc. London, Ser. A*, 1956, **235**, 67–77.
- 17 J. H. Knox and I. H. Grant, *Chromatographia*, 1987, **24**, 135–143.
- 18 J. H. Knox, *Chromatographia*, 1988, **26**, 329–337.
- 19 A. Cifuentes and H. Poppe, *Chromatographia*, 1994, **39**, 391–404.
- 20 M. R. Doshi, P. M. Daiya and W. N. Gill, *Chem. Eng. Sci.*, 1978, **33**, 795–804.
- 21 K. D. Dorfman and H. Brenner, *J. Appl. Phys.*, 2001, **90**, 6553–6554.
- 22 Y. Wang, Q. Lin and T. Mukherjee, *Lab Chip*, 2004, **4**, 453.
- 23 S. K. Griffiths and R. H. Nilson, *Anal. Chem.*, 2000, **72**, 5473–5482.
- 24 J. H. Knox and K. A. McCormack, *Chromatographia*, 1994, **38**, 207–214.
- 25 R. F. Probstein, *Physicochemical Hydrodynamics: An Introduction*, 2nd edn., John Wiley & Sons, New York, 2003.
- 26 Y. Wang, Q. Lin and T. Mukherjee, *Proceedings of 2002 Symposium on Micro Total Analysis Systems (MicroTAS '02)*, Nara, Japan, 2002, pp. 82–84.
- 27 J. C. Giddings, *Unified separation science*, Wiley, New York, 1991.
- 28 F. Foret, M. Deml and P. Bocek, *J. Chromatogr.*, 1988, **452**, 601–613.
- 29 E. B. Cummings, S. K. Griffiths, R. H. Nilson and P. H. Paul, *Anal. Chem.*, 2000, **72**, 2526–2532.
- 30 www.comsol.com.
- 31 Q. Lin, F. Jiang, X. Wang, Z. Han, Y. C. Tai, J. Lew and C. M. Ho, *Technical Digest of 2000 Solid-State Sensor and Actuator Workshop (Hilton Head 2000)*, Hilton Head Island, SC, USA, 2000, pp. 304–307.